Electron affinities of ^{16}O, ^{17}O, ^{18}O, the fine structure of $^{16}O^-$, and the hyperfine structure of $^{17}O^-$

C. Blondel, C. Delsart, C. Valli, and S. Yiou*
Laboratoire Aimé-Cotton, Centre National de la Recherche Scientifique, Bâtiment 505, F-91405 Orsay cedex, France

M. R. Godefroid and S. Van Eck
Laboratoire de Chimie Physique Moléculaire, Université Libre de Bruxelles, Code Postal 160/09, 50, avenue F.D. Roosevelt, B 1050 Bruxelles, Beligum

(Received 30 March 2001; published 8 October 2001)

Photodetachment microscopy has been used in a double-pass, field-collinear scheme in order to measure the electron affinity of atomic oxygen. As an illustration of the sensitivity of the method, electron images could be recorded even from the rarest $^{17}O^-$ ion. Analysis of photodetachment images recorded with this odd isotope, however, requires that one knows the unresolved hyperfine structures of the ground states of both the neutral atom ^{17}O and the negative ion. Calculation of the hyperfine structure of $^{17}O^-$ was achieved, which permitted to add the electron affinity of ^{17}O to the series of the measured electron affinities of oxygen isotopes. The anomalous isotope shift of these electron affinities is finally compared with *ab initio* calculations.

DOI: 10.1103/PhysRevA.64.052504 PACS number(s): 32.10.Hq, 32.10.Fn, 32.80.Gc, 31.30.Gs

I. FIELD-COLLINEAR DOUBLE-PASS PHOTODETACHMENT MICROSCOPY AS A TOOL FOR ELECTRON AFFINITY MEASUREMENTS

A. Principle of the experiment

1. The photodetachment microscope as an electron spectrometer

Photodetachment microscopy, as explained in recent papers [1,2], consists in looking at the spatial distribution of electrons that are released from an atomic anion in a photodetachment process, in the presence of an electric field. Because of the presence of the field, the outgoing, negatively charged, electron wave is constrained along the direction of the electric field. At the very beginning of the escape motion, however, half of the electron wave is emitted upfield and it undergoes subsequent reflection by the electrostatic force. An interference then occurs between two nearly equal halves of the wave. The electron spot, though strongly localized around the electric field axis, is thus not a classical distribution, but an electron interference pattern.

Photodetachment of a single, or even a few ions does not lead to the observation of the pattern, for a few detection events cannot make but a set of scarce impacts, distributed apparently at random. It is only when making statistics becomes possible, i.e., when several thousand electrons have appeared on the detector that the interference pattern becomes visible [3]. Since the detection probability of the electron is proportional to the squared modulus of the electron wave function in the atomic anion-excited state, the observed interference pattern can be considered as a direct view of the internal atomic wave function. This is the reason why, following the idea of the theorists who had first suggested the experiment [4], the device has been named a photodetachment microscope.

The electron interference pattern brought to observation by photodetachment microscopy is very sensitive to the initial energy ϵ with which the electron has been released. More precisely, the number of rings in this pattern varies as $\epsilon^{3/2}$ [2], which must be compared to the slower variation, with an $\epsilon^{1/2}$ law, of the diameter of the electron spot itself. Moreover, determination of the number of rings, i.e., the phase of the interferogram, can be made without knowing the actual size of the pattern, which makes the measurement free of all the uncertainties related to the absolute scale of the detector. Both factors explain why the photodetachment microscopy images can be used to measure electron kinetic energies with an accuracy increased by several orders of magnitude with respect to classical electron spectrometry. In essence, the accuracy reached is that of an electron interferometer [2].

2. Electron affinity measurements

Once the photodetached electron energy ϵ is known, and provided that one knows the energy $h\nu$ of the absorbed photon, subtracting the former from the latter in principle gives a very direct access to the detachment energy, i.e., the electron affinity of the studied atomic species. The photodetachment microscopy method, when performed on a negative ion beam, however, suffers from the bad knowledge that we have of the photon energy, as seen from the ion frame. The acceleration voltage U of the ion beam is typically between 100 and 500 V, which corresponds to velocities between 35 and 77 km s^{-1}. At such velocities, an uncertainty of 1° on the crossing angle of the laser and ion beams still reflects itself in several hundredth of a cm^{-1} with the apparent photon energy.

Because photodetachment microscopy takes place in the presence of a nonzero electric field F, it is actually difficult to know the actual direction of flight of the ion beam at the place where it is illuminated with more than a 1° accuracy. The Doppler shift undergone by the detaching photon must

*Present address: Institut d'optique théorique et appliquée, F-91403 Orsay, France.

then be considered as an additional unknown to the experimentalist.

One has known for many years how to deal with the existence of such an additional unknown. If the Doppler shift at one laser-ion beam crossing cannot be known directly, one can send the laser back parallel to itself, so as to make a second, Doppler-symmetric laser-ion interaction experiment. Such a double pass method was used 12 years ago to measure the electron affinity of fluorine by a classical laser-photodetachment-at-threshold (LPT) experiment [5]. Averaging the two apparent threshold values automatically eliminates the first-order Doppler shift. The higher-order $\gamma = 1/\sqrt{1-(v^2/c^2)}$ factor of the Doppler shift, which is angle independent, can then be eliminated in a satisfactory way with only a rough estimate of the ion velocity v.

An older LPT measurement of the electron affinity of oxygen [6] was also performed in this way, in the special configuration of collinear spectroscopy, which makes the Doppler shifts produced in both parallel and antiparallel cases extreme, thus giving the additional advantage of a minimum broadening. Moreover, the Doppler shifts of parallel and antiparallel experiments are such that geometrical averaging makes it possible to eliminate the Doppler shift to all orders without even knowing the ion velocity [7]. Applying this mathematical trick to the 1985 data led to a slight revision of the electron affinity of oxygen [8]. Parallel and antiparallel collinear LPT spectroscopy was still used, most recently, to measure the electron affinity of potassium [9].

The double-pass scheme was used in a first attempt to measure a detachment threshold by photodetachment microscopy two years ago [10]. In order to maintain a good spatial resolution at the second ion-laser interaction zone, the laser had to be refocused onto the ion beam. This had led us to reorient the light beam orthogonal to both the ion beam and electric field. A loss of spatial resolution resulted in one direction of the detection plane, which did not prevent us, however, to count the interference fringes and measure in this way the detachment threshold of the ion under study [10].

3. The case of oxygen

Among other technical reasons that had led us to choose O^-, one was that, at the time, the electron affinity of oxygen had been the most accurately known of all atomic electron affinities [11]. Actually the measured electron affinity has been a puzzle for the last two years, for the new technique yielded 11 784.682(20) cm^{-1} [10], whereas the admitted figure had been 11 784.648(6) cm^{-1} [6,11,8]. Incompatibility of the two measurements immediately raised the question of the validity of photodetachment-microscopy-based electron affinity measurements. This induced us to use a smaller curvature concave mirror, which made it possible to set the laser beams back in a direction quasiparallel to the electric field, as depicted in Fig. 1, and recover the original quality of the electron images. The result of the new, more accurate, measurement of the electron affinity of ^{16}O performed in this way is one of the experimental results of the present paper. Not only was the quality of the images improved, but a larger number of them was recorded too. In addition, despite the very weak natural abundance of the minor isotopes 17 and 18, photodetachment images of the corresponding ions could also be recorded, thus leading to a complete set of data for the electron affinities of all three natural isotopes of oxygen.

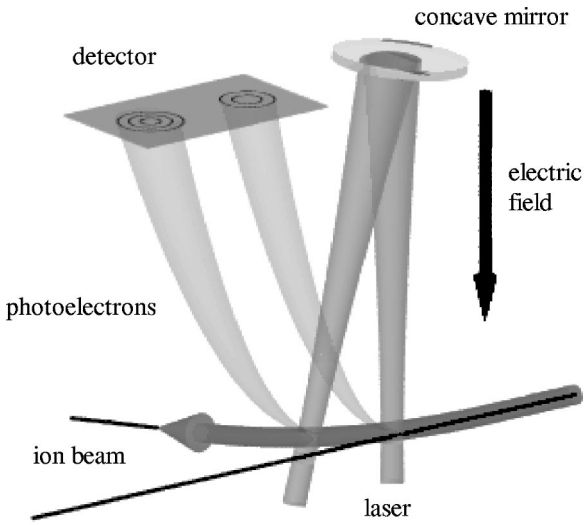

FIG. 1. Scheme of the experimental setup used for double-pass field-collinear photodetachment microscopy. A 0.85 m concave mirror is used to focus the laser beam back onto the ion beam. The distance D between the two photodetachment ring patterns equals the distance between the two interaction zones. Angles have been exaggerated, but the angle between the two laser directions is actually of the same order of magnitude as the deflection of the ion beam by the electric field.

B. Quantitative analysis

1. Images from a pointlike source

An example of a pair of images obtained with the set-up shown in Fig. 1 is given in Fig. 2. Photodetachment is produced by the same titanium-sapphire laser as in our previous O^- detachment experiment [2]. The laser power lies between 0.8 and 1.1 W, which leads, when focused in the interaction region, to an illumination of the ions of the order of 1.7×10^9 W m^{-2}. The electric field amplitude, in an electromagnetic wave of such power, is about 1.2×10^6 V m^{-1}, which is only 2.3×10^{-6} a.u. (atomic units) and should not induce any appreciable light shift, nothing more than a few 10^{-8} eV.

All electron images obtained so far could be fitted by the theoretical electron current distribution expected from a pointlike monoenergetic electron source [12,13,2]. Actually, the question was whether rescattering of the electron wave by the atomic neutral core could produce some deviation from this model. If such a process takes place, one can imagine that it scatters a fraction of the field-reflected half-wave into a new term of the spherical outgoing electron wave. The corresponding phase correction, in the interferogram, will go through zero every time the phase difference of the interfering half-waves is a multiple of 2π. The global phase of the interferogram should not be affected, on average, but the fringe profiles could become asymmetric. We have not observed any effect of this kind.

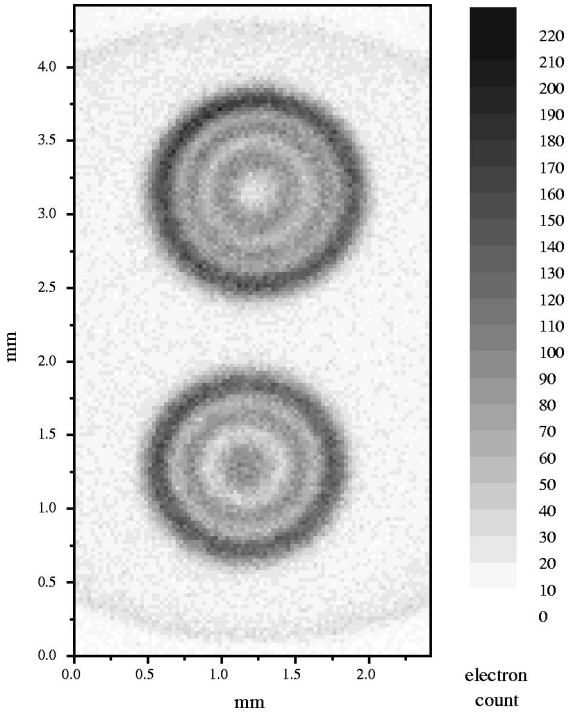

FIG. 2. A photodetachment double spot from $^{16}O^-$, in a field $F \simeq 536$ V m^{-1}. Detection takes place 0.514 m away from the laser-ion crossings. The ion kinetic energy is 500 eV. There is of course only one laser frequency, but the Doppler shift is larger for the incoming laser beam (top spot) than for the reflected laser beam (bottom spot), which results in initial electron kinetic energies of 0.980 and 0.863 cm^{-1}, respectively, and the observed differences in the ring patterns. The electron affinity deduced from this very pair of spots is 11 784.679(1) cm^{-1}, which shows the accuracy of the fitting procedure. Other sources of uncertainties have to be taken into account, which make the final error bar of the electron affinity larger (see text). Rainbows can be observed, at the top and bottom of the image, which are due to more energetic electrons detached from fine-structure excited $^{16}O^-$.

The scattering phase, by the way, is likely to be rendered very small by the smallness of the electron initial kinetic energy. The electron wave vector k_0 at the origin being only a few 10^{-3} a.u., only a huge scattering length a_S would make it possible for the $k_0 a_S$ product to reach measurable values. But a recent estimate of the e-O scattering length [14] has shown it to be only about 1/4 in atomic units. This makes anyway the scattering cross-section (smaller than 1 a.u. $\simeq 2.8\times 10^{-21}$ m^2) much smaller than the surface on which the field-reflected electron half-wave spreads (8×10^{-13} m^2 in the example of Fig. 2) at the atom level. This already shows how small the fraction of rescattered electron current will be.

Moreover, a description of photodetachment in the presence of an electric field, at low energies above threshold, has included rescattering effects to check for their possible influence on the total photodetachment cross sections [14]. Such an influence had been suspected from photodetachment experiments on S^- and Cl^- [15]. The conclusion is that rescattering effects, in that experiment, were quite small. Since the scattering length for the e-O is even smaller than for the e-Cl and e-S systems, and given the fact that we work in a smaller field too, one can definitely expect rescattering effects to be negligible in our experiment.

2. Electron image fitting

The fitting procedure of the photodetachment microscopy patterns is a least-square fit of every two-dimensional image by a calculated distribution obtained from the theoretical one after convolutions that reflect the finiteness of our spatial and spectral resolutions. Both spatial and spectral broadenings must actually be taken into account, because they affect the images in different ways. Spatial broadening, due first to the finite 65 μm full width at half maximum (FWHM) resolution of the detector [16] and, second, to the imperfect focusing of the detaching laser will reduce the fringe contrast the more where the fringe interval is smaller, i.e., more at the outer part of the ring pattern. Spectral broadening, which induces a slight variation of the outermost ring radius, has a more sensitive effect at the center of the image, where the $\epsilon^{3/2}$ variation of the phase makes the central ring, or spot, shift accordingly.

Free parameters in the fitting procedure are the background electron flux, the global amplitude of the detached electron current, the position of the image, its distortion from the perfect circular shape, the global size of the spot, the characteristic widths for spatial and spectral broadening, and, last but not least, the initial kinetic energy ϵ of the electron. All of these parameters cannot practically be let free simultaneously. For instance, the coordinates of the center of the spot are adjusted first without making any convolution of the ideal image. The obtained values then serve as a basis for further adjustment of the more valuable experimental parameters, and finally of ϵ itself.

Since the scale of the electron spot is let free all through the fitting procedure, the actual size of the electron spot serves as no constraint to the other fitting parameters. This contrasts with the classical electron spectrometry method that would on the contrary rely on the absolute radius of the spot as a measure of the initial velocity of the electron. Here ϵ is not constrained to give the spot a definite size, but the right number of rings N or, more strictly speaking, the right phase $\Phi = 2\pi N$ to the interferogram, which is such as

$$\Phi = \frac{4\sqrt{2}}{3}\frac{\sqrt{m}}{\hbar q F}\epsilon^{3/2} \tag{1}$$

with q the elementary electric charge.

Formula (1) shows that the method we use to analyze photodetachment electron images in fact produces a measure of the ratio $\epsilon^{3/2}/F$. Deducing the value of ϵ from that ratio, we shall never obtain a relative accuracy better than two-thirds of the uncertainty of our F measurement. Uncertainty about the actually applied electric field thus remains the most fundamental source of uncertainty in our electron spectrometry method.

3. Electron affinity extraction

If the two photodetachment spots were produced by parallel, counterpropagating laser beams, and ignoring second-

order Doppler terms, the detachment threshold E_a of the ion under study could be very directly deduced from the initial kinetic energies ϵ and ϵ' measured in the two symmetrically Doppler-shifted experiments by the formula

$$E_a = h\nu - \frac{\epsilon+\epsilon'}{2}. \tag{2}$$

The ratio of the distance D between the spots to the radius of curvature R of the reflecting mirror gives a measure of how the incident and reflected laser beams deviate from perfect antiparallelism. In the transverse configuration [10], formula (2) was modified accordingly into

$$E_a = \gamma\left(1+\beta\frac{D}{2R}\right)h\nu - \left(\frac{\epsilon+\epsilon'}{2}\right) \tag{3}$$

with, as usually, $\beta = v/c$ and $\gamma = (1-\beta^2)^{-1/2}$.

When the detaching laser beams are set quasiparallel to the electric field, deflection of the ion beam itself between the two interaction zones now takes place in the plane that they define. The deflection angle $DF/2U$ has to be introduced in the electron affinity formula, which becomes

$$E_a = \gamma\left[1+\beta\frac{D}{2}\left(\frac{1}{R}-\frac{F}{2U}\right)\right]h\nu - \left(\frac{\epsilon+\epsilon'}{2}\right). \tag{4}$$

Both formulas (3) and (4), with D an absolute, i.e., positive distance, apply to the ''upstream'' configuration where the reflected laser beam impinges on the ion beam upstream of the first interaction zone. The converse ''downstream'' case, with a reflected beam directed downstream back onto the ion beam, can be taken into account by changing the sign of either D or the ion velocity.

Since both R^{-1} and F/U are typically of the order of 1 m^{-1}, a configuration in which the angle of the laser beams at reflection would be exactly compensated by the ion beam deflection is not unrealistic. Formula (4) would then get simplified back into a simple $E_a = \gamma h\nu - ([\epsilon+\epsilon']/2)$. No special advantage is to be expected from such a situation, however, and the same level of accuracy can be reached, in principle, in any angular configuration of the laser and ion beams.

The effects just described are not just theoretical ones. The wave-number correction that results from ion beam deflection $(v/c^2)(DF/4U)\nu$ can be of the order of 2×10^{-3} cm^{-1}. This is large enough to make a significant discrepancy appear between upstream and downstream measurements, if forgotten.

Though it has so appeared only through its negative role of making the electron affinity formula more complicated, ion beam deflection is actually not just a parasitic effect, that one could think of eliminating. The idea of a photodetachment microscopy experiment on an undeflected ion beam would even lead to a paradox: measuring the neutral atom recoil momentum, one could measure the initial momentum of the electron and determine its path among the two interfering ones, without disturbing the interference pattern. It is fortunate that the ion beam gets deflected even between the emission times of the electron trajectories that interfere. Actually, as explained in Appendix A the neutral recoil momentum, taking the continuous transfer of momentum from the field to the ion or electron into account, is exactly the same whatever trajectory the electron has followed.

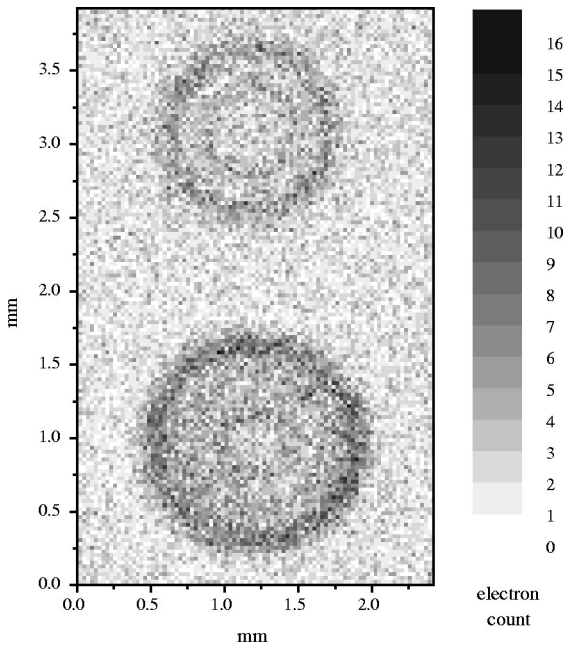

FIG. 3. A photodetachment double spot obtained from $^{17}O^-$, in a field $F \simeq 425$ V m^{-1}, after an accumulation time of 3000 s. Here the spot produced by the reflected laser beam is the top one. Despite the much smaller number of detected electrons, (16 on the most illuminated pixels) the fitting procedure remains relatively accurate, yielding 11 784.626(2) cm^{-1} for the electron affinity of ^{17}O, but the dispersion among the three recorded pairs of spots makes the statistical uncertainty larger (see Table II).

4. Hyperfine complications

Details of the ion-beam production have been given elsewhere [2,10]. Of importance here is the fact that a Wien velocity filter, set just after the ion source, gives us a mass-selectivity good enough to isolate every isotope of O^-, as it comes out of the ion source that is oxygen fed with natural N_2O. The electron affinity of ^{18}O, the natural abundance of which is 0.204%, could be measured quite in a similar way as the electron affinity of ^{16}O. Isotope ^{17}O has an even lower natural abundance of only 0.037% [17], which obliged us to accumulate the electron current for nearly an hour to get an exploitable image, whereas 10 min had been enough for each of the standard ^{16}O pictures. One of the few recorded ^{17}O double spots is given by Fig. 3.

Another difficulty occurs. The ^{17}O nucleus has a 5/2 spin, which gives both the negative ion and the neutral atom a hyperfine structure (hfs), as represented in Fig. 4. At the source and room temperatures, all hyperfine levels of $^2P_{3/2}{}^{17}O^-$ are populated in proportion to their degeneracy, and the energy of the laser photon is high enough to set any of the hyperfine levels of $^3P_2{}^{17}O$ within reach of the detachment process. The obtained detachment images are thus sta-

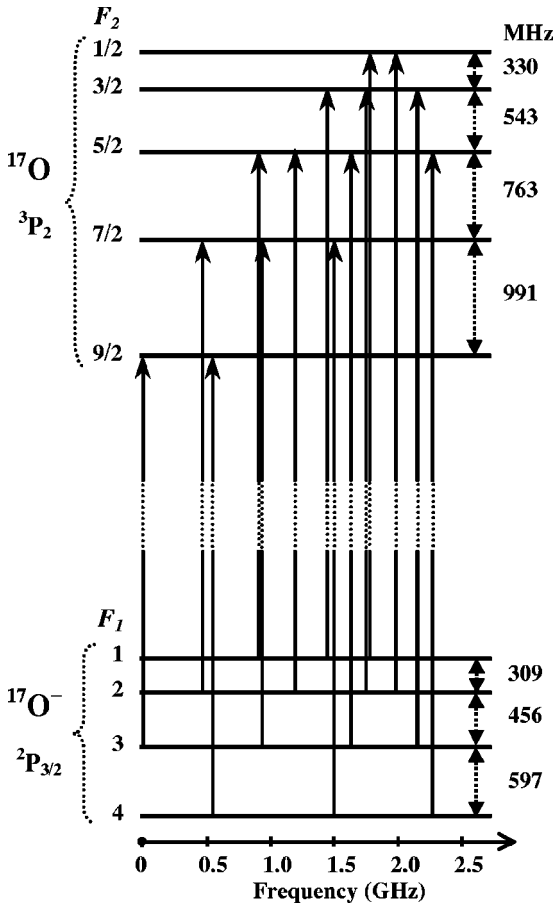

FIG. 4. Scheme of the hyperfine structure of the negative ion $^{17}O^-$ and the neutral atom ^{17}O, with the 14 electric dipole allowed detachment transitions.

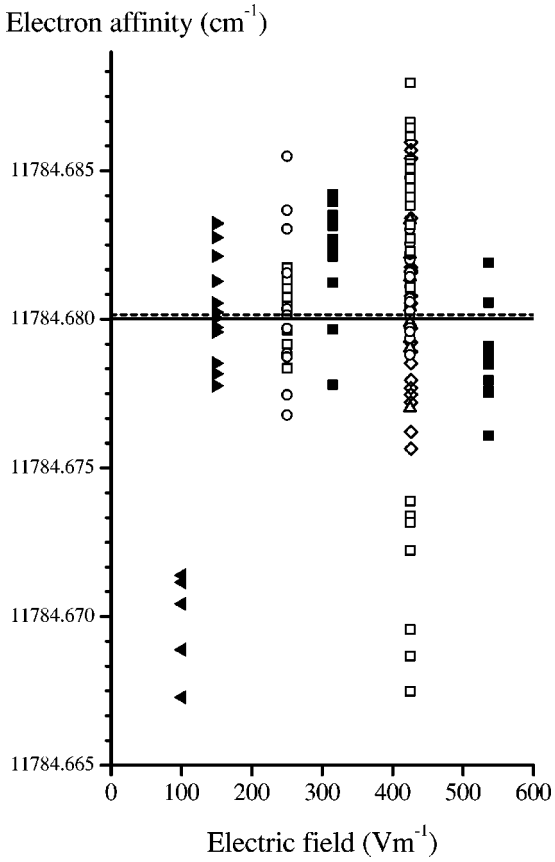

FIG. 5. Statistical dispersion of the complete set of measurements of the electron affinity of ^{16}O, sorted by the intensity of the applied electric field. The data are represented by different symbols according to the kinetic energy of the detached ions: squares stand for 500 eV, ◇ 400 eV, ○ 300 eV, △ 250 eV, ▷ 150 eV, and ◁ 100 eV. The horizontal continuous line shows the weighted average of all 141 measurements. The dashed line shows how this is modified if the lowest field data (◁100 eV) are ignored.

tistical mixtures of 14 different electron images that correspond to all detachment schemes allowed by the electric dipole transition rule. We must accordingly fit the experimental image with a sum of images calculated for 14 different kinetic energies. The statistical weighting of these 14 components obeys standard angular momentum algebra. Details of the calculation are given in Appendix B.

Last but not least, while the hfs of the $^3P_2$ ground level of ^{17}O has been well known for years [18], the hfs of $^{17}O^-$ has never been measured. A rough estimate of a negative ion hfs can nevertheless be obtained by a method that was tested with some success on $^{33}S^-$ [19]. It consists, as it is, of extrapolating the unknown hfs of $^{17}O^-$ from the known hfs of the isoelectronic ^{19}F neutral atom, with two corrective factors: (i) the ratio of the nuclear moments (ii) the ratio of the measured fine structures, which gives the variation of the $\langle r^{-3}\rangle$ factor that enters both fine- and hyperfine-structure Hamiltonians. The latter ratio is always less than one, because the electron orbitals are more loosely bound in the negative ion than the isoelectronic neutral. As a matter of fact, negative ion fine structures are found to be systematically smaller than the respective fine structures of the isoelectronic neutral atoms [20]. The estimation results in an A factor, for the hfs of ground-state $^{17}O^-$, roughly equal to -127 MHz. A firmer basis for the ^{17}O electron affinity measurement is given by the complete calculation, which is the subject of Sec. II. It takes the quadrupole effects into account, and shows the hfs of $^{17}O^-$ to be actually somewhat larger than the above estimated structure.

C. Results

1. Electron affinities

Figure 5 shows the position of the results obtained after 141 independent measurements of the electron affinity of ^{16}O. The weighted average of all measurements is 11 784.6800 cm^{-1}. If, however, the set of measurements obtained for the lowest field value 101 V m^{-1} is excluded, the weighted average appears to be a little higher, namely, 11 784.6802 cm^{-1}. The observed anomaly at 101 V m^{-1} may be due to the higher sensitivity of low-field interferograms to spurious electric or magnetic fields. The difference between the average electron affinities obtained with and without the lowest-field data does not, however, appear significant.

Table I summarizes the results of the electron affinity measurements performed on all three natural isotopes of

TABLE I. Fractional part of the photodetachment-microscopy determined electron affinities of the natural isotopes of oxygen, to be added to 11 784 cm^{-1}.

Isotope	Transverse [10]	Axial (present work)	Final
^{16}O	0.682(20)	0.680(17)	0.680(16)
^{17}O[a]	not measured	0.629(22)	0.629(22)
^{18}O	0.612(29)	0.605(20)	0.606(20)

[a]The electron affinity $E_a(17)$ of ^{17}O is the energy difference between the ground $F=9/2$ state of the neutral and the ground $F=4$ state of the ion. For the sake of calculating the isotope shift, or for gross calculations that need not take the hyperfine structure into account, the hyperfine averaged electron affinity $E_{a\mathrm{ha}}(17)$, i.e., the energy difference between the centers of gravity of both hyperfine structures is better suited. Numerically, $E_{a\mathrm{ha}}(17)=E_a(17)+0.0178\approx 11\,784.647(22)$ cm^{-1}.

oxygen by photodetachment microscopy. The final figure takes both the former ''transverse'' [10] and the present ''axial'' (i.e., field-axial) measurements into account.

The uncertainty budget is given by Table II. The physical origin of the uncertainties that limit the precision of photodetachment-microscopy determined electron affinities has been described in detail previously [10]. Of interest for the use of the data is the fact that the final error bar must include uncertainties of three kinds.

The first, and most conspicuous uncertainty results from the directly visible fluctuation of independent measurements. Averaging the measured values decreases the uncertainty because the standard deviation of the average will roughly decrease as the inverse square root of the number of measurements. The standard deviation does not, however, constitute an error bar large enough to set an interval of complete confidence. The standard deviation was thus multiplied by a large confidence factor to yield the statistical part of the error bar, which can be considered as the intrinsic accuracy limit of the photodetachment microscopy method.

Yet visible fluctuations of the results do not necessarily reveal the kind of permanent error that can be produced, e.g., by an improperly measured laser wavelength. This error can change, however, with slow variations of the lambdameter settings. The corresponding error cannot thus be described as a completely systematic one, and we shall name it a ''varying'' error.

Finally, the electric field measurement error is essentially due to the geometry of the electrodes, the spacing of which cannot be known with an infinite accuracy. This is really a systematic uncertainty. It disappears when electron affinity differences are calculated, as in isotope shifts or negative ion fine structure determinations.

TABLE II. Error budget in the present electron affinity measurements (unit: 1 mk$\equiv 10^{-3}$ cm^{-1}).

Uncertainties	Statistical[a]	Varying	Systematic	Total
^{16}O	9	3	5	17
^{17}O	14	3	5	22
^{18}O	12	3	5	20

[a]The statistical uncertainty, in order to give a real confidence interval, is set always greater than twice the standard deviation.

Some redundancy can of course exist between the three considered kinds of error. For instance, the ''varying'' error, if it varies often enough, will already contribute to the recorded fluctuations. However, the confirmed discrepancy between the present result 11 784.680(16) cm^{-1} and the formerly measured 11 784.648(6) cm^{-1} [6,8] electron affinity of ^{16}O obliges us to remain extremely careful, and better overestimate the uncertainties than take any risk of overconfidence. As a result, it must be emphasized here that our ± 16 mk error bar is not an average deviation but, in principle, a full confidence interval.

In the absence of a third measurement that would definitely settle the case, the last review of atomic electron affinities [20] recommends an intermediate value of 11 784.664(22) cm^{-1}, i.e. 1.461 112(3) eV, for ^{16}O. This mean value was chosen so as to encompass both our and the former results and gives the user the best guarantee that the actual electron affinity of oxygen lies within the given limits. We agree with that figure completely.

2. Fine structure

Photodetaching the $^{16}O^-$ ion from its $^2P_{1/2}$ fine-structure upper state makes it possible to measure the negative ion fine structure. Subtracting the apparent threshold of 11 607.596(18) cm^{-1} from the ground-state detachment energy and taking advantage of the elimination of systematic errors makes it possible to determine the fine structure interval of $^{16}O^-$ with a better accuracy than the detachment energies themselves. Numerically $\Delta E(^2P_{1/2}-{}^2P_{3/2}) \simeq 177.084(14)$ cm^{-1}. This confirms the former measurement of 177.085(27) cm^{-1} [10] by reducing its uncertainty by nearly a factor of 2. If one still wants to take the older measurement [6,11] into account, this should lead to a slight reduction of the recommended value, from 177.10(4) [20] down to 177.09(2) cm^{-1}.

II. THEORY OF THE ISOTOPE SHIFT OF ELECTRON AFFINITIES AND THE HYPERFINE STRUCTURE OF $^{17}O^-$

A. Isotope shift: A new comparison between theory and experiment

A comparison of the measured electron affinity 18-16 isotope shift with the result of calculations was already published in 1999 [21]. A first evaluation of the quality of the electronic wave functions can be made from a comparison of the electron affinities themselves. Such a comparison with other theoretical approaches was presented in Ref. [21]. Since then, an important publication by de Oliveira *et al.* [22] has appeared on the subject, focusing on a benchmark *ab initio* and density functional study of the electron affinities of the first- and second-row atoms. The *ab initio* results, which have been obtained by a combination of coupled cluster with all single, double, and triple excitations and full configuration interaction (CI) electron correlation methods,

TABLE III. Isotope shifts of the electron affinity of oxygen (in cm^{-1}).

Isotopes	Calculated	Former exp [10]	Present exp
$^{18\text{-}16}O$	-0.0573	-0.070(27)	-0.074(18)
$^{18\text{-}17}O$	-0.0269		-0.041(22)
$^{17\text{-}16}O$	-0.0304		-0.033(19)

correspond to an electron affinity value for oxygen $E_a = 1.4607$ eV, to be compared with the multiconfiguration Hartree-Fock Breit-Pauli (MCHF+BP) value of $E_a = 1.4704$ eV reported by Godefroid and Froese-Fischer [21]. The fine structure of the negative ion was already considered in Ref. [21] using the Breit-Pauli approximation, giving a fine-structure splitting of 178.33 cm^{-1} to be compared with the observed value of 177.09(2) cm^{-1} (see Sec. I C 2). The benchmark calculations of de Oliveira *et al.* [22], limited to scalar relativistic effects approximated by the first-order perturbation correction of the Darwin and mass-velocity terms, produce a slightly higher fine-structure splitting of 179.0 cm^{-1}.

The isotope shift on the electron affinity was not considered in Ref. [22]. We will refer to the paper of Godefroid and Froese-Fischer [21] for the details of the calculations of the electronic wave functions and correlation models, together with the theory of the normal mass shift and specific mass shift (SMS) contributions. The consideration of the ^{17}O isotope in the present paper allows us to introduce two new isotopic pairs, i.e., $^{18-17}O$ and $^{17-16}O$. The same computational procedure has been used for these pairs, adopting the atomic masses from the tables of Audi and Wapstra [23] for the three isotopes. The field shift due to the finite nuclear size is small for light atoms [24] and is neglected. The negative isotope shift from which an ''anomalous'' isotope shift arises, i.e., a smaller electron affinity for the heavier isotope, is observed for the three isotope pairs included in the comparison (see Table III). It reveals a strong SMS contribution induced by electron correlation, counteracting the normal mass shift. For ^{17}O, the hyperfine structures, though considered in the next section, are neglected in the theoretical estimation of the electron affinity. The comparison is made in the same table with the latter experimental data that include the hyperfine-structure averaged electron affinity of ^{17}O and the improved figures for the even isotopes. The theoretical estimations are systematically smaller than the experimental values but fall within the quoted error bars.

B. Hyperfine structure in ^{17}O and $^{17}O^-$

As explained in Sec. I B 4, the detachment images are statistical mixtures of the 14 different electron images corresponding to the electric-dipole allowed detachment processes. The hfs of the $^3P_2$ ground level of ^{17}O are known from the paramagnetic resonance experiments of Harvey [25]. This experimental hyperfine structure has been confirmed by De Natale *et al.* [18] using tunable far-infrared spectroscopy for investigating the $^3P_2$-$^3P_1$ fine-structure transitions in isotopically enriched samples of oxygen. The hyperfine structure of the $2p^4\,^3P$ ground state in ^{17}O has been evaluated theoretically by Jönsson and Godefroid [26] using multiconfiguration Hartree-Fock and configuration interaction methods. An extensive comparison with other theories and observation can be found in that reference.

The role of this section is to give the details of the theoretical estimation of the hyperfine structure parameters of the ground-level $^2P_{3/2}$ of the negative ion $^{17}O^-$. The wave functions used in the present paper are those that have been calculated by Godefroid and Froese-Fischer [21] for estimating the oxygen electron-affinity and its isotope shift. The hyperfine structure parameters of the ground state of neutral oxygen are also considered to confirm the adequacy of the correlation models used in Ref. [21].

1. Theory of ab initio hyperfine structures

The theory underlying multiconfiguration Hartree-Fock calculations of hyperfine structure parameters can be found in Ref. [27]. The diagonal magnetic dipole ($M1$) hyperfine interaction constant A_J can be defined through the first-order energy correction

$$E_{M1}(J,I,F) = \tfrac{1}{2} A_J C \tag{5}$$

with

$$A_J = \frac{\mu_I}{I} \frac{1}{[J(J+1)(2J+1)]^{1/2}} \langle \gamma_J J \| \mathbf{T}^{(1)} \| \gamma_J J \rangle \tag{6}$$

and

$$C = F(F+1) - J(J+1) - I(I+1).$$

Similarly, the diagonal electric quadrupole ($E2$) interaction parameter B_J is related to the corresponding first-order energy shift by

$$E_{E2}(J,I,F) = B_J \frac{\frac{3}{4} C(C+1) - I(I+1)J(J+1)}{2I(2I-1)J(2J-1)} \tag{7}$$

with

$$B_J = 2Q \left(\frac{J(2J-1)}{(J+1)(2J+1)(2J+3)} \right)^{1/2} \langle \gamma_J J \| \mathbf{T}^{(2)} \| \gamma_J J \rangle. \tag{8}$$

The nuclear quantities, i.e., the nuclear magnetic dipole μ_I and electric quadrupole Q moments, are defined by

$$\mu_I = \langle \gamma_I I I | M_0^{(1)} | \gamma_I I I \rangle \tag{9}$$

and

$$Q = 2 \langle \gamma_I I I | M_0^{(2)} | \gamma_I I I \rangle, \tag{10}$$

respectively. The electronic contributions can be obtained by integrating the following irreducible spherical tensors

TABLE IV. Hyperfine structure parameters (in MHz) of the $2p^4\,^3P$ states of ^{17}O.

$A(^3P_2)$	$A(^3P_1)$	$A(^3P_{2,1})$	$A(^3P_{1,0})$	Ref.
-218.0	5.63	-132.9	-102.1	MCHF+CI [26]
-217.4	6.28	-133.8	-104.6	This work[a]
-218.569(4)	4.738(36)	-126.6(2.0)	-91.7(7.2)	Obs. [25]
$B(^3P_2)$	$B(^3P_1)$	$B(^3P_{2,1})$	$B(^3P_{2,0})$	Ref.
-10.46	5.23			MCHF+CI [26]
-10.51	5.26	-2.63	-4.55	This work[a]
-10.438(30)	5.199(90)			Obs. [25]

[a]Evaluated with the wave functions of Ref. [21] corresponding to the $n=7g$ orbital active set.

$$\mathbf{T}^{(1)}=\frac{\alpha^2}{2}\sum_{i=1}^{N}\left\{2\mathbf{l}^{(1)}(i)r_i^{-3}-g_s\sqrt{10}[\mathbf{C}^{(2)}(i)\times\mathbf{s}^{(1)}(i)]^{(1)}r_i^{-3}+g_s\frac{8}{3}\pi\delta(\mathbf{r}_i)\mathbf{s}^{(1)}(i)\right\} \tag{11}$$

and

$$\mathbf{T}^{(2)}=-\sum_{i=1}^{N}\mathbf{C}^{(2)}(i)r_i^{-3} \tag{12}$$

over the spin and spatial electron coordinates. The rank-one tensor represents the magnetic field due to the electrons at the site of the nucleus arising from the orbital motion of the electrons (orbital term), from the dipole field due to the spin motion of the electrons (spin-dipole term), and the Fermi contact contribution that appears only for *s* electrons. The rank-two tensor is the electric field gradient at the site of the nucleus that ultimately interacts with the nuclear quadrupole moment to bring about the electric quadrupole hyperfine interaction.

For cases in which the hyperfine *J* mixing has to be taken into account, one needs to go beyond the first-order energy perturbation scheme by considering the hyperfine coupling between *J* levels having the same *F* value,

$$E_{M1}(J,I,F;J',I,F)=\langle\gamma_J\gamma_I JIFM_F|\mathbf{T}^{(1)}\cdot\mathbf{M}^{(1)}|\gamma_J'\gamma_I J'IFM_F\rangle, \tag{13}$$

$$E_{E2}(J,I,F;J',I,F)=\langle\gamma_J\gamma_I JIFM_F|\mathbf{T}^{(2)}\cdot\mathbf{M}^{(2)}|\gamma_J'\gamma_I J'IFM_F\rangle. \tag{14}$$

These off-diagonal matrix elements can be derived explicitly [27] for the following coupling cases:

$$E_{M1}[J,I,F;(J-1),I,F]=\tfrac{1}{2}A_{J,J-1}[(K+1)(K-2F)(K-2I)(K-2J+1)]^{1/2}, \tag{15}$$

$$E_{E2}[J,I,F;(J-1),I,F]=B_{J,J-1}[(F+I+1)(F-I)-J^2+1]\frac{[3(K+1)(K-2F)(K-2I)(K-2J+1)]^{1/2}}{2I(2I-1)J(J-1)}, \tag{16}$$

$$E_{E2}[J,I,F;(J-2),I,F]=B_{J,J-2}[6K(K+1)(K-2I-1)]^{1/2}\frac{[(K-2F-1)(K-2F)(K-2I)(K-2J+1)(K-2J+2)]^{1/2}}{2I(2I-1)J(J-1)(2J-1)} \tag{17}$$

with

$$K=I+J+F.$$

In light atoms where the relativistic effects can be neglected, the diagonal and off-diagonal *A* and *B* hyperfine interaction constants can be expressed in terms of the *J*-independent hyperfine parameters a_l, a_{sd}, a_c, and b_q defined as follows [27,28]:

$$a_l=\langle\gamma LSM_LM_S|\sum_{i=1}^{N}l_0^{(1)}(i)r_i^{-3}|\gamma LSM_LM_S\rangle, \tag{18}$$

$$a_{sd}=\langle\gamma LSM_LM_S|\sum_{i=1}^{N}2C_0^{(2)}(i)s_0^{(1)}(i)r_i^{-3}|\gamma LSM_LM_S\rangle,$$

$$a_c=\langle\gamma LSM_LM_S|\sum_{i=1}^{N}2s_0^{(1)}(i)r_i^{-2}\delta(r_i)|\gamma LSM_LM_S\rangle,$$

$$b_q=\langle\gamma LSM_LM_S|\sum_{i=1}^{N}2C_0^{(2)}(i)r_i^{-3}|\gamma LSM_LM_S\rangle,$$

where $M_L=L$ and $M_S=S$.

2. Hyperfine structure of neutral oxygen

The diagonal and off-diagonal *A* and *B* hyperfine structure parameters, evaluated with the wave functions of Godefroid and Froese-Fischer [21] (MCHF expansions corresponding to the $n=7g$ active set), are compared in Table IV with the most recent theoretical estimation of Jönsson and Godefroid

TABLE V. Convergence study of hyperfine structure parameters (in a.u.) of $2p^5\,^2P$ in $^{17}O^-$.

AS	a_l	a_{sd}	a_c	b_q
HF	4.058 0066	-0.811 6013	0.000 0000	1.623 2027
3	3.764 9016	-0.846 3192	2.875 5555	1.415 6942
4	3.811 7626	-0.858 0383	0.933 8162	1.446 7706
5	3.755 2558	-0.873 7998	0.653 3066	1.393 9440
6g	3.728 6559	-0.875 5699	0.759 3193	1.372 4817
7g	3.709 7472	-0.873 1888	0.890 4539	1.356 0459

[26] and with the experimental values determined from the paramagnetic resonance experiments of Harvey [25].

Though both calculations are based on the orbital-active-set concept in which the property is monitored as a function of the size of the one-electron orbital set spanning the configuration space, the correlation models used in Ref. [26] differ from those adopted in Ref. [21] focusing on the estimation of the electron-affinity. In Ref. [26], the MCHF expansions correspond to all single (S), double (D), triple (T), and quadruple (Q) excitations from the reference configuration to the $n=3$ active set, augmented by SD to larger active sets including up to h electrons. The effect of further TQ excitations has been investigated by configuration interaction. In Ref. [21], correlation models, limited to g orbitals, were developped in the MCHF scheme with the aim of getting the right correlation balance between the neutral atom and the negative ion. An inspection of Table IV shows that the agreement between the two approaches and with observation is satisfactory. The largest disagreement with observation appears for the diagonal parameter $A(^3P_1)$, suffering from strong cancellation between the (orbital + contact) and spin-dipole terms, as shown in Ref. [26].

3. Hyperfine structure of the negative ion

The hyperfine structure of the ground state of the negative ion is investigated for the first time in the present work.

In Table V, the J-independent hyperfine parameters are monitored as improving the wave function through extending the orbital active set (AS). While the orbital (a_l), spin-dipole (a_{sd}), and electric field gradient (b_q) parameters show a smooth convergence, the contact (a_c) term suffers of large oscillations.

The diagonal (J,J) and off-diagonal (J,J') magnetic dipole and electric quadrupole hyperfine interaction constants, A and B, are reported in Table VI and Table VII, respectively, for the different active sets. The $n=7gr$ results reported for the diagonal parameters have been obtained using the relativistic J-dependent eigenfunctions of the Breit-Pauli Hamiltonian calculated in Ref. [21]. The interaction parameter A has been calculated using nuclear spin $I=5/2$ and $\mu=-1.893\,79(9)\ \mu_N$ [29]. To compute the electric quadrupole constants B from the electric field gradient b_q we have used the semiempirical value $Q=-25.58(22)$ mb that was obtained by combining the measured B constant for $2p^4\,^3P_2$ of neutral oxygen with the electric field gradient theoretical value from finite-element MCHF calculations [30], as discussed in [26]. The contact term is definitely the most difficult to capture and the less converged contribution. As shown by Table VI, the spin-dipole term counteracts the (orbital + contact) contributions for the $J=3/2$ fine structure component. Hopefully, the cancellation is much weaker than the one found for $2p^4\,^3P_1$ of neutral oxygen [26]. For the $J=1/2$ component, the contact term is small comparatively to the large orbital and spin-dipole contributions that interfere positively. The worst interference case occurs for the off-diagonal $A_{3/2,1/2}$ parameter for which the spin-dipole and contact contributions counterbalance the orbital term. The convergence of the electric field gradient at nucleus is satisfactory but is not yet achieved for the larger orbital active sets considered in [21], as already illustrated through the

TABLE VI. Hyperfine structure parameters A (in MHz) of the $2p^5\,^2P$ states of $^{17}O^-$.

AS	$A_{\rm orb}$	A_{sd}	$A_{\rm cont}$	$A_{\rm tot}$
		1/2-1/2		
HF	-391.057 2046	-391.510 6354	0.000 0000	-782.567 8400
3	-362.811 6026	-408.258 2937	46.238 2428	-724.831 6534
4	-367.327 4510	-413.911 4745	15.015 5407	-766.223 3848
5	-361.882 0693	-421.514 7228	10.505 0131	-772.891 7791
6g	-359.318 7243	-422.368 6240	12.209 6725	-769.477 6758
7g	-357.496 5519	-421.219 9899	14.318 2853	-764.398 2565
7gr	-358.981 2490	-422.436 2732	14.242 8517	-767.174 6705
		3/2-3/2		
HF	-195.528 6023	39.151 0635	0.000 0000	-156.377 5388
3	-181.405 8013	40.825 8294	-46.238 2428	-186.818 2148
4	-183.663 7255	41.391 1475	-15.015 5407	-157.288 1188
5	-180.941 0347	42.151 4723	-10.505 0131	-149.294 5754
6g	-179.659 3621	42.236 8624	-12.209 6725	-149.632 1722
7g	-178.748 2759	42.121 9990	-14.318 2853	-150.944 5622
7gr	-178.842 0408	42.181 2512	-14.364 3035	-151.025 0931
		3/2-1/2		
HF	-97.764 3012	48.938 8294	0.000 0000	-48.825 4717
3	-90.702 9006	51.032 2867	46.238 2428	6.567 6289
4	-91.831 8627	51.738 9343	15.015 5407	-25.077 3877
5	-90.470 5173	52.689 3404	10.505 0131	-27.276 1639
6g	-89.829 6811	52.796 0780	12.209 6725	-24.823 9306
7g	-89.374 1380	52.652 4987	14.318 2853	-22.403 3540

TABLE VII. Hyperfine structure parameters B (in MHz) of the $2p^5\,^2P$ states of $^{17}O^-$.

AS	$B_{3/2,3/2}$	$B_{3/2,1/2}$
HF	9.756 0924	2.112 2560
3	8.508 8842	1.842 2274
4	8.695 6659	1.882 6669
5	8.378 1569	1.813 9241
6g	8.249 1598	1.785 9955
7g	8.150 3741	1.764 6077
7gr	8.174 2972	

convergence pattern of the J-independent hyperfine parameters (see Table V). The $A(^2P_{3/2}) = -151.0$ MHz *ab initio* value is sensitively larger than the -127 MHz found by scaling the hyperfine structure of the isoelectronic ^{19}F neutral atom, as discussed in Sec. I B 4.

The hyperfine structures of $^2P_{3/2}$ are evaluated with the *ab initio* hyperfine parameters corresponding to the largest active set $(n=7g)$, by diagonalizing the interaction matrix built from equations (5) and (7) for the diagonal matrix elements and equations (15)–(17) for the off-diagonal J-coupling terms. The experimental fine structure has been used for setting the zero-order interaction matrix. The corresponding energy differences $\Delta E_{F-F'} = E_{F'} - E_F$ between adjacent hyperfine structure components are calculated to be $\Delta E_{4-3} = 597$ MHz, $\Delta E_{3-2} = 456$ MHz, and $\Delta E_{2-1} = 309$ MHz, corresponding to an inverted hyperfine multiplet (negative A) as displayed in Fig. 4.

The departure from the Landé interval rule is small, the ratio of the hyperfine energy separations $(\Delta E_{4-3}:\Delta E_{3-2}:\Delta E_{2-1}) = (1.94:1.48:1.00)$, to be compared with the ideal theoretical ratio $(2:\frac{3}{2}:1)$ expected for a pure electric magnetic dipole first-order energy shift. Because $I=5/2$ for the ^{17}O nucleus, the off-diagonal hyperfine coupling between the $J=3/2$ and $J=1/2$ fine structure levels manifests itself only for the $F=2$ and $F=3$ hyperfine components while the $F=4$ and $F=1$ states remain pure. For these $F=2,3$ hyperfine components, the coupling between the $J=3/2$ and $J=1/2$ fine structure levels is found to be small, producing a shift of only 1.9 kHz on the $F=3$ level. Note that the effect of this off-diagonal coupling on the eigenvalue problem, which scales as the ratio $A^2_{J,J'}/(E_{J'} - E_J)$ in the perturbation regime, is larger in the hyperfine structure of neutral oxygen by roughly two orders of magnitude, due to the sensitively larger $A_{J,J'}$ interaction terms. Much more important for the negative ion is the $E2$ diagonal contribution relatively to the $M1$ diagonal contribution that affects the hyperfine structure splittings by 6.5 MHz for the ΔE_{4-3} and ΔE_{2-1} intervals. The departure from the Landé interval rule for $^{17}O^-$ mentionned above is then due to this electric quadrupole interaction, while the $(M1+E2)$ J-hyperfine mixing can be neglected, at least at the level of accuracy of our theoretical estimation.

III. CONCLUSION

The electron affinity of all three natural isotopes of oxygen could be measured by photodetachment microscopy. The measurement of the electron affinity of ^{17}O was made possible thanks to an original calculation of the hyperfine structure of $^{17}O^-$. The hyperfine averaged electron affinity of ^{17}O lies well at the expected intermediate position between the affinities of ^{16}O and ^{18}O, and confirms the negative specific mass shift predicted by calculation.

The absolute value of the electron affinity of ^{16}O is found again to be significantly higher than the value that had been measured by studying the energy variation of the total detachment cross section in the vicinity of the threshold, in 1985. Taking this fact into account, a slightly increased value of the electron affinity of oxygen was recommended, in the last review of binding energies in atomic negative ions [20]. This new value of 11 784.664(22) cm^{-1} also received carefully reevaluated error bars.

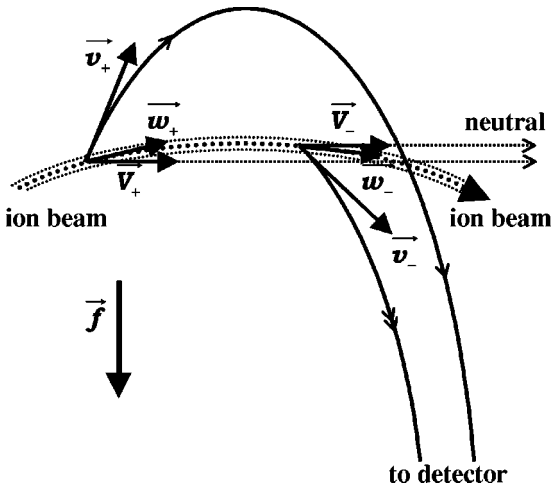

FIG. 6. Possible trajectories of the interfering electron. For the sake of clarity, the bending of the ion beam has been exaggerated, for the same force $\vec{f}$ acts on either the electron or the much heavier ion. Vectors $\vec{v}$, $\vec{V}$, and $\vec{w}$ at the time of detachment are the velocities of the electron, the atom, and the center of mass, respectively.

Further investigation is needed to understand the origin of the dispersion of photodetachment-microscopy measured electron affinities. One aim could be to study bigger ions, in order to check about the absence, or insignificance, of neutral core rescattering. Photodetachment microscopy, which has already demonstrated its ability to characterize the photodetachment of even very rare ions, could then reach within few years a less than ± 10 mk accuracy for the determination of electron affinities and fine structures of negative ions.

ACKNOWLEDGMENTS

We wish to acknowledge the help of Fabienne Goldfarb for adapting the fitting program to the multithreshold case. This research was supported in part (M.R.G.) by the Belgian National Fund for Scientific Research.

APPENDIX A: ABSENCE OF A NEUTRAL RECOIL PARADOX

A simple calculation shows what the velocity of the residual neutral atom is, after the electron has been emitted either to the upper or to the lower interfering trajectories, drawn in Fig. 6. Let $\vec{v}_\pm$ be the starting electron velocity along the upper and lower trajectories, respectively. Let $\vec{V}_\pm$ be the velocity of the residual neutral atom at the same point. We shall denote by $\vec{w}_\pm$ the velocity of the center of mass, i.e., the velocity of the ion just before detachment,

$$(M+m)\vec{w}_\pm = M\vec{V}_\pm + m\vec{v}_\pm . \tag{A1}$$

If T is the elapsed time between the relevant detachment events, with $\vec{f}$ the electrostatic force acting on the electron, when made free, or on the ion as well, we have

$$(M+m)\vec{w}_- = (M+m)\vec{w}_+ + \vec{f}T. \tag{A2}$$

Rewriting Eqs. (A2) with (A1), we have

$$M\vec{V}_- + m\vec{v}_- = M\vec{V}_+ + m\vec{v}_+ + \vec{f}T. \tag{A3}$$

But we are in the regime where detection takes place so far from the interaction zone that we can consider it to occur at infinity, where the electron velocities have to be equal (for the slightest velocity mismatch, when multiplied by infinity, would prevent the trajectories from hitting the detector simultaneously). If the final electron velocities are equal, the initial electron velocities differ only due to the difference in time of flight,

$$m\vec{v}_- = m\vec{v}_+ + \vec{f}T. \tag{A4}$$

Setting Eq. (A4) into Eq. (A3) yields, after simplification

$$\vec{V}_- = \vec{V}_+, \tag{A5}$$

which means that, whatever the time of emission, the velocity of the emitted neutral is the same. This shows how illusory, in this far-field detection scheme (where only the momenta of the particles are measured), the idea of detecting the neutral atom angle of emission was, supposedly to determine which of the two paths the interfering electron had gone through. There is actually only one common emission angle, and no neutral recoil paradox at all.

APPENDIX B: BRANCHING RATIOS OF THE HYPERFINE COMPONENTS FOR *S*-WAVE PHOTODETACHMENT—APPLICATION TO THE $^2P_{3/2}$-$^3P_2$ DETACHMENT THRESHOLD OF $^{17}O^-$

1. Standard calculation

The relative contributions of the hyperfine components of a detachment threshold can be calculated from different points of view. The first, or standard method, considers the process: Negative ion ground state + laser photon $\mapsto$ atom ground state + low-energy electron.

Assuming pure L-S and I-J couplings, we describe a hyperfine state of the negative ion ground level by the ket vector $|\alpha_1(S_1L_1)J_1,I,F_1\rangle$ (initial state) and we shall represent a hyperfine state of the atom ground level by the bra vector $\langle\alpha_2(S_2L_2)J_2,I,F_2|$. The ejected electron of spin $s=1/2$, angular momentum l couples as $(sl)j$ and the final states of the process will be represented on the basis of $\langle\alpha_2[(S_2L_2)J_2I]F_2,(sl)j,F|$ vectors. For oxygen, due to the effect of the Wigner law [31] in the vicinity of the photodetachment threshold, $l=0$ and $j=1/2$.

The relative intensity $I(F_2,F_1)$ of a hyperfine component is to be calculated using the reduced electric dipole matrix elements from initial-state F_1 to final-state F and then summing squared amplitudes over all possible values of F and j,

$$I(F_2,F_1) = \sum_{F,j} |\langle[(S_2L_2)J_2I]F_2,(sl)j,F\|r^{(1)}\|(S_1L_1)J_1,I,F_1\rangle|^2 = \sum_{F,j} |a(F_2,j,F,F_1)|^2, \tag{B1}$$

where $r^{(1)}$ is a spherical tensor of rank 1. Summation over all possible projections M is implicit.

According to standard Racah algebra and notations (three-angular momentum coupling) [32], the final state can be expanded in terms of states resulting from the coupling $(J_2j)J$,

$$\langle(J_2I)F_2,j,F| = \sum_J (-)^{j+J_2+I+F}[J,F_2]^{1/2}\begin{Bmatrix} I & F & J \\ j & J_2 & F_2 \end{Bmatrix} \times\langle(J_2,j)J,I,F|. \tag{B2}$$

We can then reduce the new matrix elements with the standard formula [32]

$$\langle J,I,F\|r^{(1)}\|J_1,I,F_1\rangle = (-)^{J+I+F_1+1}[F,F_1]^{1/2}\begin{Bmatrix} F & 1 & F_1 \\ J_1 & I & J \end{Bmatrix} \times\langle J_2,j,J\|r^{(1)}\|S_1,L_1,J_1\rangle. \tag{B3}$$

Angular momenta S and L that result from the couplings $(S_2s)S$ and $(L_2l)L$ can be used to uncouple the spin and orbit of the state $\langle J_2,j,J|$ (four-angular momentum coupling) [32]

$$\langle(S_2L_2)J_2,(s,l)j,J| = \sum_{S,L} [J_2,j,S,L]^{1/2}\begin{Bmatrix} S_2 & L_2 & J_2 \\ s & l & j \\ S & L & J \end{Bmatrix} \times\langle S,L,J|. \tag{B4}$$

Let us note that the electric dipole operator does not act on the spin so that $S_1=S$, and there is no sum over S in the intensity calculation. The remaining reduced matrix elements $\langle S,L,J\|r^{(1)}\|S_1,L_1,J_1\rangle$ are straightforwardly calculated [32],

$$\langle S_1,L,J\|r^{(1)}\|S_1,L_1,J_1\rangle = (-)^{S_1+L_1+J+1}[J,J_1]^{1/2}\begin{Bmatrix} J & 1 & J_1 \\ L_1 & S_1 & L \end{Bmatrix} \times\langle\alpha_2,L\|r^{(1)}\|\alpha_1,L_1\rangle. \tag{B5}$$

Combining all these equations allows us to express $a(F_2,j,F,F_1)$ as follows:

$$a(F_2,j,F,F_1)=\sum_{L,J}(-)^{2J+S_1+L_1+j+J_2+2I+F_1+F}[J]\times[J_1,J_2,j,S_1,L,F_2,F,F_1]^{1/2}\begin{Bmatrix} I & F & J \\ j & J_2 & F_2 \end{Bmatrix}\times\begin{Bmatrix} F & 1 & F_1 \\ J_1 & I & J \end{Bmatrix}\begin{Bmatrix} J & 1 & J_1 \\ L_1 & S_1 & L \end{Bmatrix}\times\begin{Bmatrix} S_2 & L_2 & J_2 \\ s & l & j \\ S & L & J \end{Bmatrix}\langle\alpha_2,L\|r^{(1)}\|\alpha_1,L_1\rangle. \tag{B6}$$

Now we concentrate on the special case of s-wave photodetachment, which results in the following particular relations: $l=0$, $L=L_2$, $j=s$. The sum over j disappears so that

$$I(F_2,F_1)=\sum_F |a(F_2,F,F_1)|^2 \tag{B7}$$

in which the expression of $a(F_2,F,F_1)$ can be easily simplified and redistributed as follows:

$$a(F_2,F,F_1)=(-)^{2s+S_1+L_1+S_2+L_2+J_2+2I+F_1+F}\times[J_1,J_2,S_1,F_2,F,F_1]^{1/2}\langle\alpha_2,L_2\|r^{(1)}\|\alpha_1,L_1\rangle\times\sum_J(-)^{3J}[J]\begin{Bmatrix} I & F & J \\ s & J_2 & F_2 \end{Bmatrix}\begin{Bmatrix} F & 1 & F_1 \\ J_1 & I & J \end{Bmatrix}\times\begin{Bmatrix} J & 1 & J_1 \\ L_1 & S_1 & L_2 \end{Bmatrix}\begin{Bmatrix} L_2 & J & S_1 \\ s & S_2 & J_2 \end{Bmatrix}. \tag{B8}$$

Standard reorganization of the 6-j symbols leads to an expression of $I(F_2,F_1)$,

$$I(F_2,F_1)=\sum_F |a(F_2,F,F_1)|^2=[J_1,J_2,S_1]|\langle\alpha_2,L_2\|r^{(1)}\|\alpha_1,L_1\rangle|^2[F_2,F_1]\sum_F[F]\times\left|\sum_J(-)^J[J]\begin{Bmatrix} I & F & J \\ s & J_2 & F_2 \end{Bmatrix}\begin{Bmatrix} s & J_2 & J \\ L_2 & S_1 & S_2 \end{Bmatrix}\times\begin{Bmatrix} L_2 & S_1 & J \\ J_1 & 1 & L_1 \end{Bmatrix}\begin{Bmatrix} J_1 & 1 & J \\ F & I & F_1 \end{Bmatrix}\right|^2. \tag{B9}$$

The sum over J appears as a standard 12-j symbol except for the sign [33]. Finally, we obtain a simple and general formula, valid for s-wave photodetachment,

TABLE VIII. Contribution ratios of the 14 hyperfine subthresholds of $^{17}O^-$.

Initial F_1	Final F_2	$I(F_1,F_2)$ (%)	Total $I(F_1)$ (%)
1	1/2	2	$\frac{25}{2}$
	3/2	49/10	
	5/2	28/5	
2	1/2	14/3	$\frac{125}{6}$
	3/2	25/6	
	5/2	20/7	
	7/2	64/7	
3	3/2	64/15	$\frac{175}{6}$
	5/2	47/5	
	7/2	43/6	
	9/2	25/3	
4	5/2	15/7	$\frac{75}{2}$
	7/2	145/14	
	9/2	25	

$$I(F_2,F_1)\propto[F_2,F_1]\sum_F[F]\times\begin{Bmatrix} s & F & 1 & L_2 \\ F_2 & F_1 & L_1 & S_2 \\ J_2 & I & J_1 & S_1 \end{Bmatrix}^2, \tag{B10}$$

which implies eight triangular conditions: (S_1,L_1,J_1), (S_2,L_2,J_2), (J_1,I,F_1), (J_2,I,F_2), (S_2,s,S_1), (F_2,s,F), $(F_1,1,F)$, and $(L_1,1,L_2)$.

Application to the 14 hyperfine components of the $^{17}O^-$ ($^2P_{3/2}\rightarrow{}^3P_2$) threshold was achieved with the corresponding values [33,34]: $I=5/2$, $S_1=1/2$, $L_1=1$, $J_1=3/2$, $F_1=1-4$, $s=1/2$, $S_2=1$, $L_2=1$, $J_2=2$, $F_2=1/2$–$9/2$. Due to some of the triangular conditions, the sum over F reduces to one or two terms. Table VIII summarizes the intensity branching amounts in percent, and also the total contribution for every initial F_1 hyperfine level.

2. Fractional-parentage-based calculation

The second calculation uses a method introduced by Engelking and Lineberger to determine fine-structure branching ratios [35]. Detachment is assumed to be a direct, one-electron process, and the interaction with the laser photon "annihilates" an electron of spin $s=1/2$ and angular momentum l' by promoting it into the continuum (for instance, a p electron for oxygen). This electron couples as $(s,l')j'$. The other notations remain identical as before.

The relative intensity between the hyperfine components can be calculated through reduced matrix elements of the transition from the negative ion state F_1 to the atom state F_2

with a tensor $T^{(sl')j'}$ of rank j', and then by summing over the possible values of j'.

$$I(F_2,F_1) = \sum_{j'} |\langle \alpha_2[(S_2L_2)J_2I]F_2 \| T^{(sl')j'} \| \alpha_1[(S_1L_1)J_1I]F_1\rangle|^2. \tag{B11}$$

Uncoupling the F_i momenta reduces the matrix elements to the fine structure [32,33]

$$\langle (J_2I)F_2 \| T^{j'} \| (J_1I)F_1\rangle = (-)^{J_2+I+F_1+j'}[F_1,F_2]^{1/2} \begin{Bmatrix} F_2 & j' & F_1 \\ J_1 & I & J_2 \end{Bmatrix} \langle J_2 \| T^{j'} \| J_1\rangle. \tag{B12}$$

Then the reduced matrix elements can be expressed as

$$\langle J_2 \| T^{j'} \| J_1\rangle = \langle \alpha_2(S_2L_2)J_2 \| T^{(sl')j'} \| \alpha_1(S_1L_1)J_1\rangle = [J_2,j',J_1]^{1/2} \begin{Bmatrix} S_1 & L_1 & J_1 \\ s & l' & j' \\ S_2 & L_2 & J_2 \end{Bmatrix} \times \langle (S_2,L_2)l'\}S_1,L_1\rangle \langle S_2 \| t^-_{1/2} \| S_1\rangle \langle L_2 \| t^- \| L_1\rangle. \tag{B13}$$

Operators $t^-_{1/2}$ and t^- are proportional to annihilation operators that act on the spin and orbital factors of the electron state, respectively. Factor $\langle (S_2,L_2)l'\}S_1,L_1\rangle$ is a parentage coefficient for forming the ion term by adding an electron to the neutral term, its "parent."

Then, for a given $^{2S_1+1}L_1 \rightarrow {}^{2S_2+1}L_2$ transition, $I(F_2,F_1)$ is proportional to a sum,

$$I(F_2,F_1) \propto \sum_{j'=l'-s}^{j'=l'+s} [F_1,F_2,J_1,J_2,j'] \begin{Bmatrix} F_2 & j' & F_1 \\ J_1 & I & J_2 \end{Bmatrix}^2 \begin{Bmatrix} S_1 & L_1 & J_1 \\ s & l' & j' \\ S_2 & L_2 & J_2 \end{Bmatrix}^2 \tag{B14}$$

Application to the 14 hyperfine components of the $^{17}O^-$ ($^2P_{3/2} \rightarrow {}^3P_2$) threshold was achieved in the special case of the annihilation of a p electron ($l'=1$, $j'=1/2,3/2$) [34]. The intensity branching amounts in percent are given by the reduced expression,

$$I(F_2,F_1) = \frac{10}{3}[F_1,F_2] \left[\begin{Bmatrix} F_2 & 1/2 & F_1 \\ 3/2 & 5/2 & 2 \end{Bmatrix}^2 + 4 \begin{Bmatrix} F_2 & 3/2 & F_1 \\ 3/2 & 5/2 & 2 \end{Bmatrix}^2 \right]. \tag{B15}$$

Remarkably enough, the numerical results are strictly identical to those reported in Table VIII.

[1] C. Blondel, C. Delsart, and F. Dulieu, Phys. Rev. Lett. **77**, 3755 (1996).
[2] C. Blondel, C. Delsart, F. Dulieu, and C. Valli, Eur. Phys. J. D **5**, 207 (1999).
[3] A. Tonomura, J. Endo, T. Matsuda, T. Kawasaki, and H. Ezawa, Am. J. Phys. **57**, 117 (1989).
[4] Yu. N. Demkov, V. D. Kondratovich, and V. N. Ostrovskii, Pis'ma Zh. Eksp. Teor. Fiz. **34**, 425 (1981) [JETP Lett. **34**, 403 (1981)].
[5] C. Blondel, P. Cacciani, C. Delsart, and R. Trainham, Phys. Rev. A **40**, 3698 (1989).
[6] D. M. Neumark, K. R. Lykke, T. Andersen, and W. C. Lineberger, Phys. Rev. A **32**, 1890 (1985).
[7] P. Juncar, C. R. Bingham, J. A. Bounds, D. J. Pegg, H. K. Carter, R. L. Mlekodaj, and J. D. Cole, Phys. Rev. Lett. **54**, 11 (1985); M. Kaivola, O. Poulsen, E. Riis, and S. A. Lee, *ibid.* **54**, 255 (1985).
[8] C. Blondel, Phys. Scr. **58**, 31 (1995).
[9] K. T. Andersson, J. Sandström, I. Yu. Kiyan, D. Hanstorp, and D. J. Pegg, Phys. Rev. A **62**, 022503 (2000).
[10] C. Valli, C. Blondel, and C. Delsart, Phys. Rev. A **59**, 3809 (1999).
[11] H. Hotop and W. C. Lineberger, J. Phys. Chem. Ref. Data **14**, 731 (1985).
[12] V. D. Kondratovich and V. N. Ostrovsky, J. Phys. B **23**, 3785 (1990).
[13] C. Bracher, W. Becker, S. A. Gurvitz, M. Kleber, and M. S. Marinov, Am. J. Phys. **66**, 38 (1998).
[14] I. I. Fabrikant, J. Phys. B **27**, 4545 (1994).
[15] N. D. Gibson, B. J. Davies, and D. J. Larson, Phys. Rev. A **47**, 1946 (1993).
[16] Model 3391 of Quantar Technology Inc., 200 Washington Street, Santa Cruz, CA 95060.
[17] C.M. Lederer, J.M. Hollander, and I. Perlman, *Table of Isotopes* (Wiley, New York, 1967).
[18] P. De Natale, M. Bellini, W. Goetz, M. Prevedelli, and M. Inguscio, Phys. Rev. A **48**, 3757 (1993).
[19] R. Trainham, R. M. Jopson, and D. J. Larson, Phys. Rev. A **39**, 3223 (1989).
[20] T. Andersen, H. K. Haugen, and H. Hotop, J. Phys. Chem. Ref. Data **28**, 1511 (1999).
[21] M. R. Godefroid and C. Froese-Fischer, Phys. Rev. A **60**, R2637 (1999).
[22] G. de Oliveira, J. M. L. Martin, F. de Proft, and P. Geerlings, Phys. Rev. A **60**, 1034 (1999).
[23] G. Audi and A. H. Wapstra, Nucl. Phys. A **565**, 1 (1993).
[24] W. H. King, *Isotope Shifts in Atomic Spectra* (Plenum Press, New York, 1984).
[25] J. S. M. Harvey, Proc. R. Soc. London, Ser. A **285**, 581 (1965).
[26] P. Jönsson and M. Godefroid, Mol. Phys. **98**, 1141 (2000).
[27] P. Jönsson, C.-G. Wahlström, and C. Froese-Fischer, Comput. Phys. Commun. **93**, 399 (1993).

[28] A. Hibbert, Rep. Prog. Phys. **38**, 1217 (1975).
[29] P. Raghavan, At. Data Nucl. Data Tables **42**, 189 (1989).
[30] D. Sundholm and J. Olsen, J. Phys. Chem. **96**, 627 (1992).
[31] E. P. Wigner, Phys. Rev. **73**, 1002 (1948).
[32] Lloyd Armstrong, Jr., *Theory of the Hyperfine Structure of Free Atoms* (Wiley Interscience, New York, 1971).
[33] B. Judd, *Operator Techniques in Atomic Spectroscopy* (Princeton University Press, Princeton, 1998).
[34] M. Rotenberg, R. Bivins, N. Metropolis, and John K. Wooten, Jr., *The 3-j and 6-j Symbols* (Massachusetts Institute of Technology, Cambridge, 1959).
[35] P. C. Engelking and W. C. Lineberger, Phys. Rev. A **19**, 149 (1979).